Design and simulation of a silicon-based hybrid integrated optical gyroscope system

Dao-Xin Sun(孙道鑫)[1], Dong-Liang Zhang(张东亮)[1,†], Li-Dan Lu(鹿利单)[1], Tao Xu(徐涛)[1], Xian-Tong Zheng(郑显通)[1], Zhe-Hai Zhou(周哲海)[2,‡], and Lian-Qing Zhu(祝连庆)[1]

[1] *Key Laboratory of the Ministry of Education for Optoelectronic Measurement Technology and Instrument, Beijing Information Science & Technology University, Beijing* 100192, *China*

[2] *Beijing Laboratory of Optical Fiber Sensing and System, Beijing Information Science & Technology University, Beijing* 100016, *China*

(Received 5 May 2022; revised manuscript received 11 July 2022; accepted manuscript online 18 July 2022)

By combining a silicon-based lithium niobate modulator and a silicon-based Si_3N_4 resonator with silicon-based photonics technology, a highly systematic design of a hybrid integrated optical gyroscope with enhanced reciprocity sensitivity and a dual micro-ring structure is proposed for the first time in this paper. The relationship between the device's structural parameters and optical performance is also analyzed by constructing a complete simulation link, which provides a theoretical design reference to improve the system's sensitivity. When the wavelength is 1550 nm, the conversion frequency of the dual-ring optical path is 50 MHz, the coupling coefficient is 0.2, and the radius R is 1000 μm, the quality factor of the silicon-based Si_3N_4 resonator is 2.58×10^5, which is 1.58 times that of the silicon-on-insulator resonator. Moreover, the effective number of times the light travels around the ring before leaving the micro-ring is 5.93, which is 1.62 times that of the silicon-on-insulator resonator. The work fits the gyro dynamic output diagram, and solves the problem of low sensitivity at low speed by setting the phase offset. This results provide a basis for the further optimization of design and chip processing of the integrated optical gyroscope.

Keywords: silicon photonics, integrated optical gyroscope, micro-ring resonator, Sagnac effect

PACS: 42.81.Pa, 42.82.Et, 42.82.–m, 42.82.Fv **DOI:** 10.1088/1674-1056/ac81a9

1. Introduction

An optical gyroscope is an optical sensor that measures the rate of rotation by exploiting a relativistic phenomenon known as the Sagnac effect. It is an important part of the inertial navigation system, and plays a vital role in the national defense and civil fields.[1,2] The integrated optical gyroscope uses a waveguide resonator to replace the fiber ring, and employs integrated optical process technology to realize the on-chip integration of multifunctional optoelectronic devices. It can reduce the weight and size of the gyroscope, lower the cost and power consumption, enhance the control of thermal effect, perform on-chip modulation and detection, and increase the system's reliability. Meanwhile, it illustrates significant advantages in processing repeatability, device integration, cost, and power consumption, and has important research significance.[3–5]

In recent years, various research groups have attempted to improve the performance of integrated optical gyroscopes by utilizing various materials and structural designs.[6–12] In 2011, Huaiyong[13] designed a gyroscope with a dual-resonator structure, which effectively reduced the noise caused by Rayleigh backscattering, the Kerr effect, and polarization coupling. In 2013, Ciminelli[14] proposed a three-resonator structure composed of three resonators with different radii and coupling ratios to increase the quality factor of the resonant cavity without increasing the size of the sensor, thereby effectively improving the performance of the gyroscope. In 2014, Lishuang[15] proposed a silicon-based dual-waveguide ring resonator with good long-term bias stability. The quality factor of the resonant cavity can reach up to 6.13×10^6, and the zero-bias stability obtained under 10 s integration time is 0.22 °/s. In 2018, Khial[16] proposed a silicon-based dual-resonator structure with enhanced reciprocity sensitivity. The size of the gyroscope is only 2 mm^2, the measured quality factor reaches 10^5, and a minimum phase shift of 3 nrad can be detected. In 2018, Mohammadi[17] proposed a photonic crystal resonator structure consisting of a 3 dB coupler, two bus waveguides, and five ring resonators with different radii and refractive indices to improve the coupling efficiency between the ring resonator and the waveguide, where the simulated quality factor is 4326. Progressively, in 2019, Yu[18] proposed a mode-assisted integrated waveguide interferometric gyroscope structure, which utilizes the back-propagation of two different spatial modes in the waveguide sensing coil to form a fixed phase difference to achieve high-sensitivity detection. In 2020, Daoxin[19] at Zhejiang University proposed a super-high quality factor racetrack micro-ring resonator structure, where the quality factor is as high as 2.3×10^6 theoretically. Their work provides new design ideas for high-performance silicon optical devices, and is of great signifi-

[†]Corresponding author. E-mail: zdl_photonics@bistu.edu.cn
[‡]Corresponding author. E-mail: zhouzhehai@bistu.edu.cn

© 2023 Chinese Physical Society and IOP Publishing Ltd

cance for breaking through the performance bottlenecks of important devices, such as optical filters and nonlinear devices. In addition, with the development of hybrid integration technology, silicon-based integrated light sources,[20–22] lithium niobate modulators,[23–25] and Si_3N_4 photonics[26,27] can combine the performance advantages of multiple material systems, and can further improve the performances of integrated photonics systems.

Due to the signal quality, the bandwidth, half-wave voltage, insertion loss and other key performance parameters of traditional silicon-based electro-optical modulators are limited. Meanwhile, the cavity length needs to be extended to reach a high Q value, resulting in large transmission loss and thereby low detection sensitivity. Accordingly, in this paper, based on the integrated photonic gyroscope with a reciprocity-sensitive enhanced dual micro-ring resonator architecture,[16] silicon-based lithium niobate thin film and silicon-based Si_3N_4 integrated photonics are incorporated into the integrated optical gyroscope model and a corresponding simulation link is constructed. The influence of the silicon-based Si_3N_4 dual micro-ring structure and the silicon-based lithium niobate modulator on the overall performance of the gyroscope is analyzed, and the relevant mathematical relationship between the parameters is obtained. The quality factor of our resonator reaches up to 10^5 with a cavity length of 2000 μm, and the effective number of times light travels around the ring before leaving the micro-ring is as high as 5.93 times. This study presents new ideas and references for further improvement of the performance of the new silicon-based hybrid integrated optical gyroscope.

2. Theoretical model and simulation method

As depicted in Fig. 1, when the circular optical path rotates in the inertial space around an axis perpendicular to the optical path plane (speed Ω), the two rows of light waves, propagating clockwise (CW) and counterclockwise (CCW), respectively, produce an optical path difference ΔL due to the rotation. This leads to the interference of two coherent light waves with a phase difference of $\Delta\varphi_{\text{sagnac}}$.[28] The intensity of the interference signal can be detected using a photodetector, and the angular velocity of rotation can be determined as follows:

$$\Delta\varphi_{\text{sagnac}} = \frac{8\pi n}{\lambda c} mA\Omega, \tag{1}$$

where $\Delta\varphi_{\text{sagnac}}$ is the Sagnac phase difference, n is the effective refractive index of the waveguide, λ is the wavelength, mA is the area vector with size equal to the area of the closed path multiplied by m (number of turns), Ω is the angular velocity vector, and c is the speed of light.

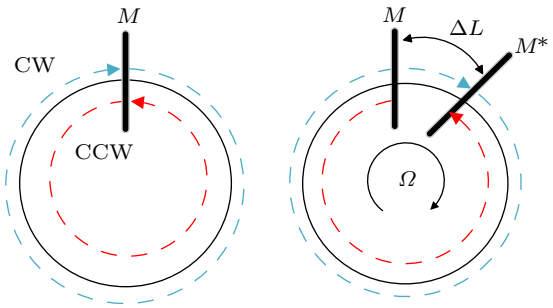


Fig. 1. A schematic diagram of the Sagnac effect.

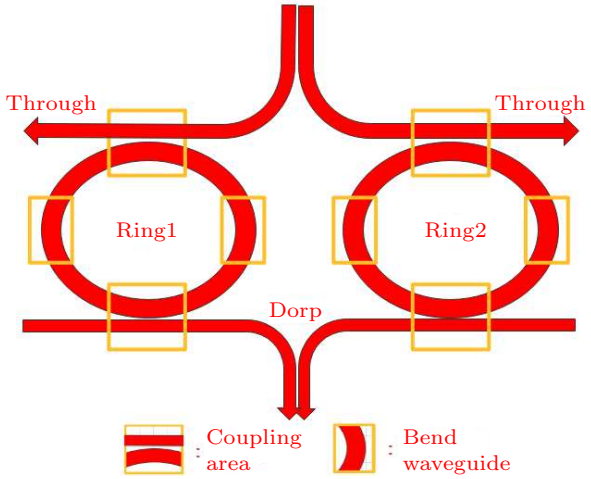


Fig. 2. A schematic diagram of the dual micro-ring resonant cavity structure.

In the study, the reciprocity-sensitive enhanced dual-micro-ring resonant architecture integrated photonic gyroscope's sensitive unit[16] is used as the theoretical model. Si_3N_4 material with low loss, large transparent bandwidth, and a negligible nonlinear absorption effect is used to construct a micro-ring waveguide platform and, by relying on this, link modeling and simulation analysis are carried out. As shown in Fig. 2, the gyro sensitive unit is composed of two racetrack-type micro-ring resonators in the form of an add-drop with the same structure. Moreover, the two micro-rings share the input signal. The main advantages of this architecture are listed as: (i) increased Sagnac phase difference via the micro-ring resonance method; (ii) by dividing the signal light (propagating clockwise and counterclockwise) into two micro-rings, any back-reflected light coupled to the back-propagation mode will not directly affect the output, thereby reducing the impact of back reflection; (iii) high-speed switching of incident light and electrical signal processing can effectively offset the thermal noise; (iv) the TiN thermal adjustment electrode can be deposited on the processed micro-ring waveguide, where the refractive index and light phase of the input waveguide and micro-ring waveguide can be modulated by the thermo-optical effect to compensate the process error.

The drop port signals of the two micro-ring resonators are coupled with each other to generate an interference signal. The

intensity of the interference signal changes with the change in rotational angular velocity of the micro-ring. By detecting the intensity change in the interference signal, the variation in rotational angular velocity can be obtained. Meanwhile, the output phase difference of the micro-ring resonator is expressed as[16]

$$\sigma_{\text{sagnac}} \approx S \times \Delta\varphi_{\text{sagnac}} = \frac{Q\lambda}{\pi n L_{\text{c}}} \Delta\varphi_{\text{sagnac}}, \tag{2}$$

where Q is the quality factor of the ring cavity, which characterizes the photon lifetime in the cavity, L_{c} is the circumference of the micro-circle, and S corresponds to the effective number of times light travels around the ring before leaving the micro-ring. The phase response of the resonant cavity in this structure amplifies the $\Delta\varphi_{\text{sagnac}}$, thereby improving the sensitivity of detection. According to formula (2), the Q value plays an important role in realizing high-precision gyroscopes, and the Q value of the resonant cavity is defined as

$$Q = 2\pi f \frac{U}{P} = -2\pi f \frac{U}{\mathrm{d}U/\mathrm{d}t} = 2\pi f \tau, \tag{3}$$

where U is the total energy in the cavity, $P = \mathrm{d}U/\mathrm{d}t$ is the loss speed of the light energy in the cavity, f is the frequency of the resonant light wave, and τ is the ring-down time of the light energy in the cavity. Here, the full width at half maximum (FWHM) method is used to calculate the quality factor of the resonant cavity, and its expression is as follows:

$$\text{FWHM} = \frac{c}{\pi L_{\text{c}} n} \cdot \frac{k^2}{\sqrt{1-k^2}}, \tag{4}$$

where k is the coupling coefficient of the coupler. It can be seen that the FWHM is proportional to the coupling coefficient k and is inversely proportional to the cavity length L_{c} of the resonator.

This work uses the Lumerical Interconnect module to build a simulation link for the optimization analysis, as demonstrated in Fig. 3. The light emitted by the laser CWL enters the optical path conversion module COMPOUND_1 through the polarization controller POL. With this module, light can be input to the dual micro-ring resonator COMPOUND_2 from the upper and lower directions, i.e., the light is transmitted in time-sharing between $\mathrm{I} \rightarrow \mathrm{I}^*$ and $\mathrm{II} \rightarrow \mathrm{II}^*$. The light output by the two micro-rings interferes and is output to the photodetector PIN, and the output current is observed by the oscilloscope OSC. Each part in Fig. 3 will be introduced and designed in detail below.

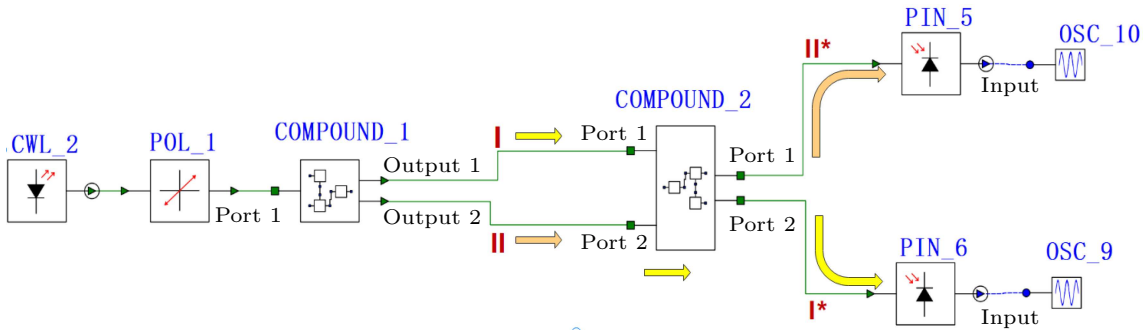


Fig. 3. The gyro system simulation design drawing.

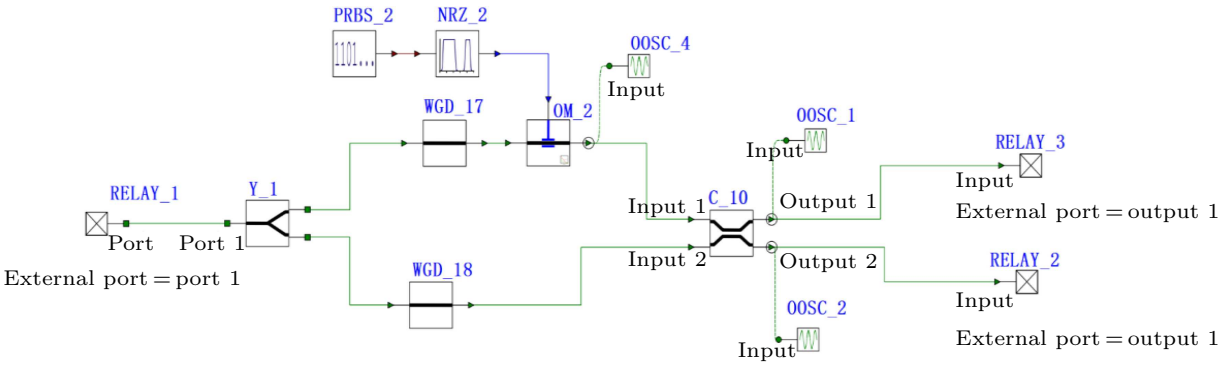


Fig. 4. The COMPOUND_1 optical path high-speed conversion module.

The optical path conversion module (COMPOUND_1 in Fig. 3) uses a hybrid integrated technology of a silicon waveguide and lithium niobate. This hybrid integrated architecture avoids the large loss of silicon-based modulators originating from carrier dispersion effects, and enables low-loss, small-size, and high-speed electro-optical modulation. As shown in Fig. 4, the link model of the optical path conversion module mainly implements the high-speed conversion of the optical

path between output 1 and output 2, through the 1×2 Mach–Zehnder interferometer (MZI) structure. The light emitted by the CWL is equally divided into two beams by the beam splitter Y_1 into the upper-arm straight waveguide WGD_17, the electro-optical modulator OM_2 and the lower-arm straight waveguide WGD_18, which are output by the coupler C_10, and the spectrum can be observed from the optical oscilloscope OOSC. In addition, OM_2 is a physical model based on a silicon-based lithium niobate electro-optical modulator.

By applying a modulation voltage to the modulator OM_2, the optical phase of one arm of the MZI is modulated. For lithium niobate material, the phase change caused by the electro-optical effect is given by[29,30]

$$\Delta\phi = \pi n_{\mathrm{e}}^3 \gamma_{33} \Gamma \frac{V_0 L}{\lambda G}, \tag{5}$$

$$n_{\mathrm{e}} = \sqrt{\left(\frac{2.9804\lambda^2}{\lambda^2 - 0.02047} + \frac{0.5981\lambda^2}{\lambda^2 - 0.0666} + \frac{8.9543\lambda^2}{\lambda^2 - 416.08} + 1\right)}, \tag{6}$$

$$\gamma_{33} = 27.04426 + \frac{7.50588}{\lambda^2 + 3.90008} + \frac{0.75161}{\lambda^2 - 0.05138}, \tag{7}$$

where n_{e} is the optical refractive index; γ_{33} is the electro-optical coefficient; Γ is the overlap integral factor, which represents the strength of interaction between the light wave field and the applied electric field and assumes the value between 0 and 1; $L = 40$ mm is the electrode length; G is the electrode gap width; and $\lambda = 1.55$ μm is the wavelength of input light. The calculated values for n_{e} and γ_{33} are 2.1376 and 28.5549, respectively. Correspondingly, the half-wave voltage is[27]

$$V_\pi = \frac{\lambda G}{n_{\mathrm{e}}^3 \gamma_{33} \Gamma L}. \tag{8}$$

Phase changes under different voltage values are calculated using formulas (5)–(8), and the corresponding relationship generation file is loaded into the OM_2 model. When the electrode modulation voltage is applied, the output spectrum of the coupler is analyzed. The voltage values corresponding to the power extreme points of the two optical paths are selected as the maximum and minimum values of the modulated square-wave driving signal, where PRBS and NRZ are used to generate the square wave. In this way, high-speed conversion of the optical path is realized and modulation of the optical path is completed.

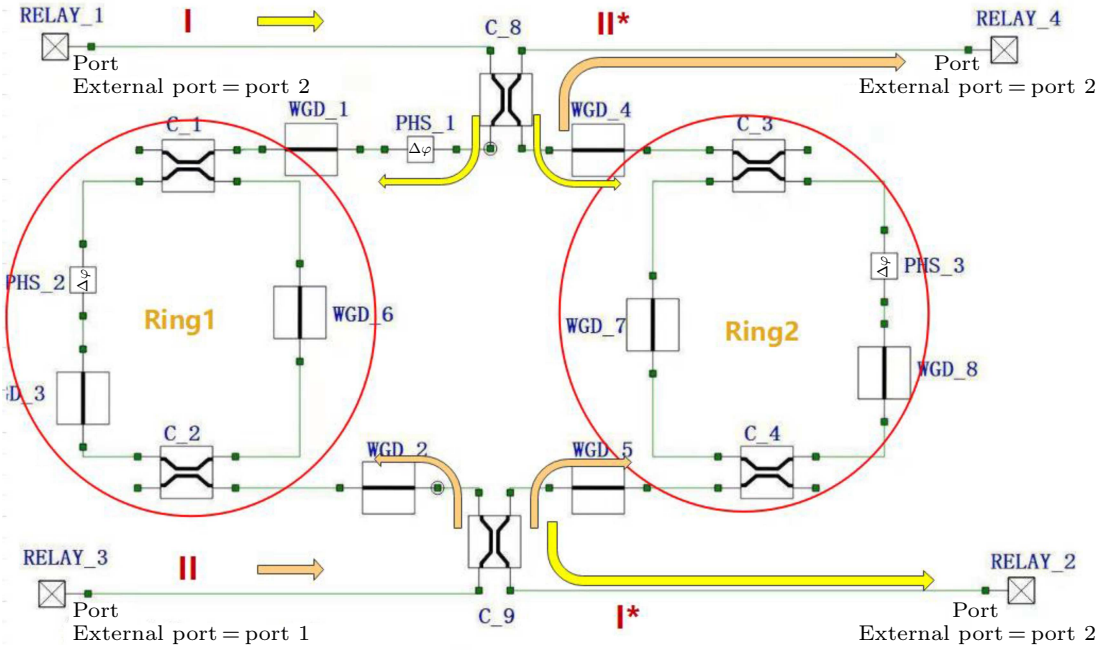


Fig. 5. A simulation link diagram of the double micro-ring resonator.

COMPOUND_2 in Fig. 3 refers to a dual micro-ring structure of the gyro sensitive unit, and figure 5 provides the link simulation model of this device. When the light needs to change its path during the process of straight waveguide transmission, choosing an appropriate bending radius is an effective way to reduce the loss. In this paper, the Lumerical MODE software module is used to simulate the transmission loss of a waveguide with a height of 0.22 μm and a width of 0.5 μm under different bending radii. It is found that when the bending radius is greater than 5 μm, the loss can be ignored. Therefore, the bending radius of the coupling region C and the bending radius of the micro-ring in this design are both greater than 5 μm. By doing so, the loss caused by the bending of the waveguide becomes negligible, and the micro-ring curved waveguide can be simply replaced by a straight waveguide WGD.

In the simulation of the rotation effect, the rotation speed is converted into the change of optical phase information,

where the phase shifter PHS is used. Every half cycle, the light path switches between I $\rightarrow$ I* and II $\rightarrow$ II*. In the first half of the cycle, I $\rightarrow$ I* corresponds to the light input from RELAY_1. After the two beams of light are equally divided between the resonators Ring1 and Ring2 from the coupler C_8, interference occurs at the coupler C_9, and then the interference signal is output from RELAY_2. Coherently, in the other half of the cycle, II$\rightarrow$II* corresponds to light input from RELAY_3, and output from RELAY_4, after passing through the dual micro-ring.

3. Simulation results and discussion

3.1. High-speed conversion optical path analysis

By simulating the link model given in Fig. 4, the input-output characteristics of the optical path conversion module are obtained, as demonstrated in Fig. 6. The ultimate goal here is to obtain a suitable square-wave voltage, to realize the optical path conversion under the square-wave driving signal, where the conversion frequency is determined by the square-wave frequency.

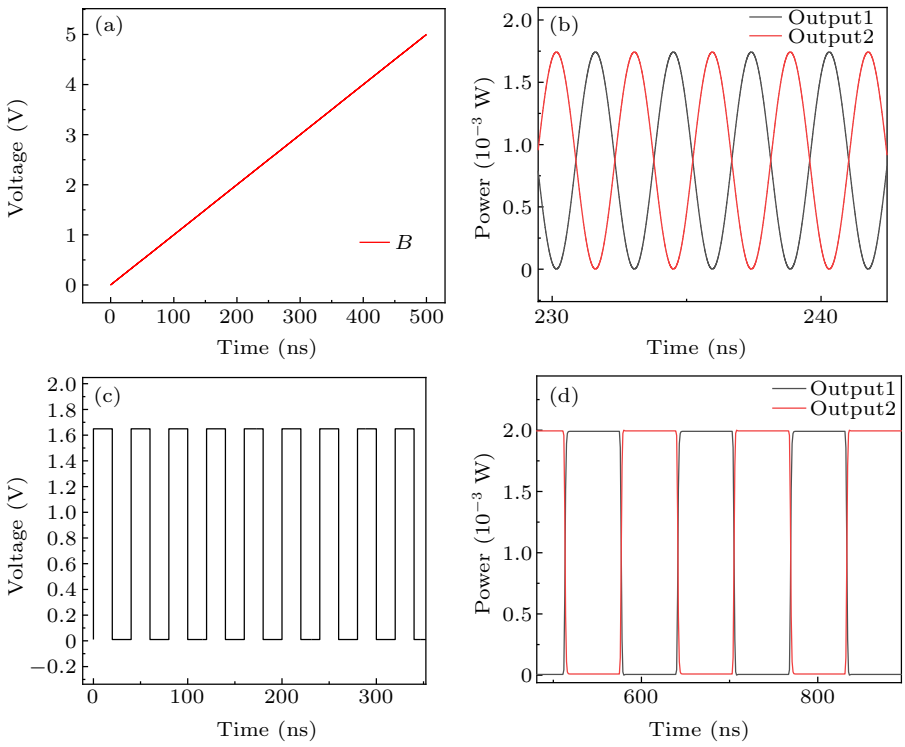


Fig. 6. Simulation results of the input–output characteristics of the optical path conversion module: (a) the linear voltage applied to the modulator electrode; (b) the corresponding output spectrum under linear voltage drive; (c) the square-wave voltage applied to the modulator electrode; (d) the corresponding output spectrum driven by a square-wave voltage.

3.2. The influence of cavity parameters on gyroscope performance

From formula (2), the output phase difference of the resonant cavity is closely related to the quality factor Q and the cavity length L_c. The following section reports the simulation and analysis of the relationships between the coupling coefficient k, cavity length L_c, Q value, and gyro output current I, through the link model presented in Fig. 5.

Initially, the output spectrum is simulated for different values of the cavity length L_c of the resonant cavity, as shown in Fig. 7, where the output spectrum is observed near the wavelength of 1550 nm. As L_c increases from 1571 μm to 6282 μm, the resonant wavelength keeps changing around 1550 nm, and the resonance depth and spectral width of the transmission spectrum decrease gradually. However, the transmission loss increases with the increase of the cavity length. As the cavity length increases and reduces the 3 dB bandwidth, the resonance peak becomes narrower, thereby indicating an increase in the Q value. In one previous study,[31] it was verified that as the transmission loss increases, the Q value decreases gradually. Compared with the silicon waveguide in the silicon on insulator (SOI), the Si_3N_4 waveguide has a smaller transmission loss; it is about 1/100 of the silicon waveguide loss. It can be seen from Fig. 8(a) that under the same cavity length, the Si_3N_4 resonator loss is smaller; therefore, the Q value is larger, and the Q value increases with the increase of the cavity length. In Fig. 8(b), the S-factor of the SOI micro-ring decreases with increasing R, while the S-factor of the Si-based Si_3N_4 resonator varies negligibly. It can be seen from formula (2) that the quality factor and the cavity length increase by the same extent at this time, and a good match is achieved. Under the same radius $R = 1000$ μm, the Q value of the Si_3N_4 resonator is 2.58×10^5, and the S factor is 5.93; the Q value of the SOI resonator is 1.63×10^5, and the S value is 3.75.

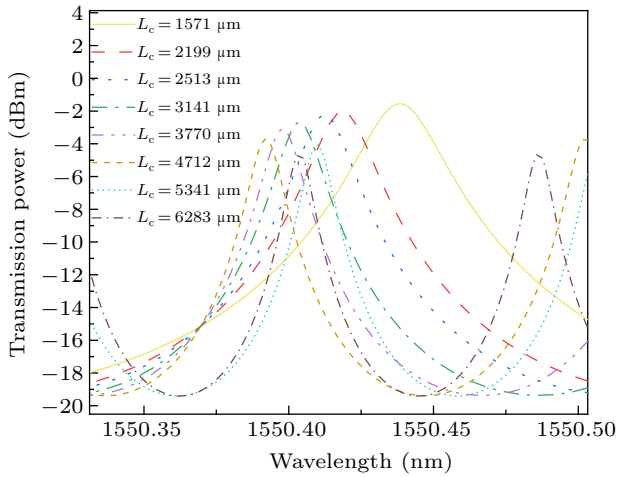


Fig. 7. Transmission spectra under different cavity lengths.

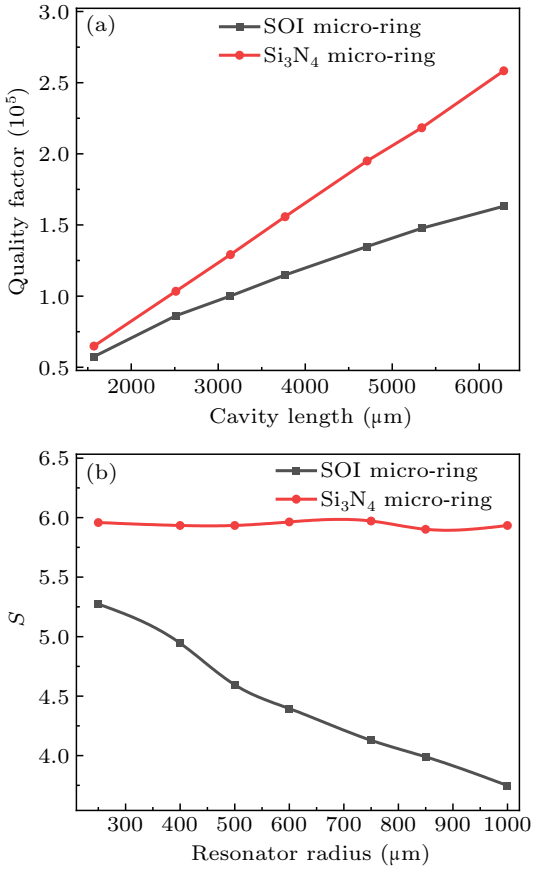


Fig. 8. Comparative analysis diagrams of the Si_3N_4 resonator and SOI resonator. (a) The relationship between cavity length and quality factor; (b) the relationship between the cavity radius and the *S* factor.

As shown in Fig. 9, when L_c is fixed, the coupling efficiency increases with the increase of the coupling coefficient k of the resonant cavity, which is equivalent to an increase in the coupling loss of the resonant cavity. As a result, the Q value gradually decreases. When the coupling coefficient k is in the range of 0.1 to 0.3, the output current shows an increasing trend, and the maximum output current value at $k = 0.3$ is the equivalent of about 1.75×10^{-4} A. The output current decreases with the increase in k from 0.3 to 0.5.

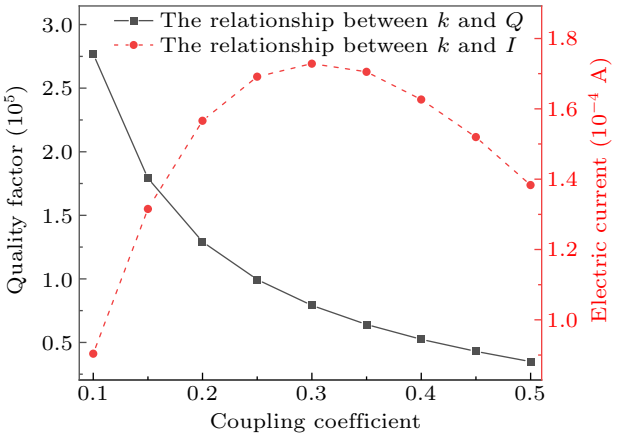


Fig. 9. The relationship between the coupling coefficient and the quality factor, and the output current.

3.3. Effect of switching frequency and offset phase on output signal

The function of dual micro-ring architecture is to suppress the thermal noise, and the frequency of optical path switching has a large influence on the noise suppression effect.[16] At the same rotating speed, when two output current signals are at different switching frequencies, the gyroscope outputs current signals, as plotted in Fig. 10. As evident from Figs. 10(a) and 10(b), when the frequency is too high, the two output currents will have obvious step fluctuations, and alternate oscillations will originate at the intersection. From Fig. 10(c), as the frequency decreases, the jitter decreases. In Fig. 10(d), when the frequency is $f = 50$ MHz, the output waveform tends to be stable. This is because the detector used in this link is an ideal model and is not limited by bandwidth. Therefore, in the dynamic simulation process, the weak change in output intensity caused by the light circulating in the micro ring can be detected by the detector. In the actual photodetector, the detection signal is the effect of time integration. Considering that the purpose of switching between upper and lower channels is to reduce the thermal noise, bandwidth reduction is conducive to reducing the system costs, and 50 MHz modulation bandwidth can meet the relevant demands. Due to difficulties when describing the thermal disturbance noise model, it is impossible to simulate and evaluate the effect of modulation frequency on noise suppression.

Based on the above analysis, the key parameters of the system simulation are selected, as shown in Table 1 below, some of which are based on my previous research.[31]

The simulation of the link is carried out according to the above system parameters, and the output current of the gyroscope under different speeds is recorded, as shown in Fig. 11. If the output signal of PIN is processed directly when the speed is low, the corresponding $\Delta\varphi$ tends to 0. At this time, $\mathrm{d}I/\mathrm{d}\varphi$ reaches 0, the signal detection sensitivity is the lowest, and the low-speed signal cannot be demodulated accurately. More-

over, this function relationship is an even function with symmetry, and the direction of the phase shift is difficult to determine: that is, the direction of rotation cannot be determined, as indicated by the red curve. Therefore, this research proposes to introduce a phase offset into the resonant cavity to improve the sensitivity: that is, add a $\pi/2$ phase offset to the PHS_1 position in Fig. 5. Through simulation, the relationship between the output current and rotation speed is extracted, as shown by the black curve in Fig. 11. The data shows that by setting the offset phase, the problem of indeterminate rotation speed and low sensitivity is solved, the output current is increased, and the detection range is expanded.

Table 1. Simulation parameters.

Name	Values
Power source	2 mW
Si straight waveguide width	0.5 μm
Cavity length	3141 μm
Switching frequency	50 MHz
Coupling coefficient in cavity	0.2
Coupling waveguide bend radius	5 μm
Si_3N_4 straight waveguide transmission loss	3 dB/m
Resonator waveguide width	1.2 μm
Si waveguide height	0.22 μm
Coupling length	10 μm
Y-branch splitting ratio	50:50
Half wave voltage value	1.64 V

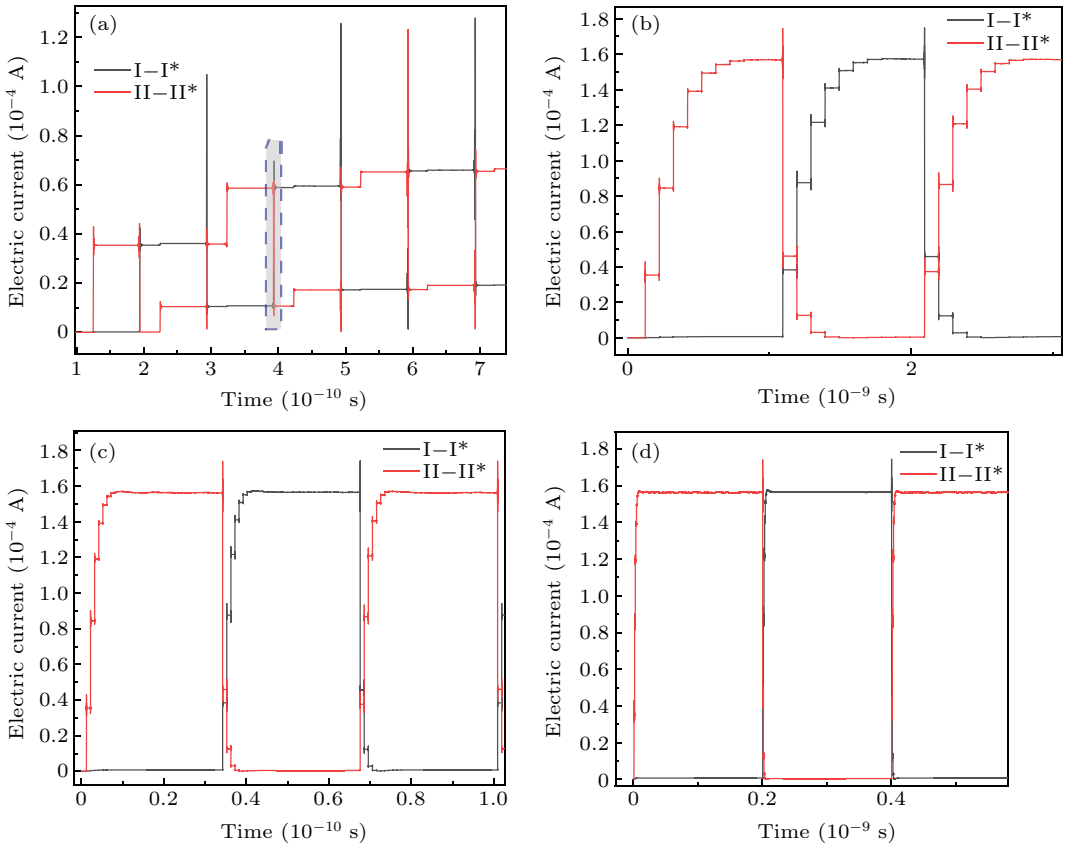


Fig. 10. Analysis of the influence of the switching frequency f on the output current signal: (a) $f = 10$ GHz; (b) $f = 1$ GHz; (c) $f = 300$ MHz; (d) $f = 50$ MHz.

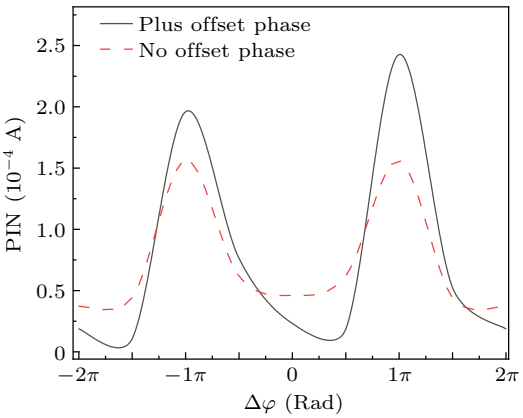


Fig. 11. The gyro dynamic output curve.

4. Conclusion

In this paper, a detailed simulation analysis of a silicon-based hybrid integrated interferometric gyroscope optical system based on a dual micro-ring architecture is carried out. The MZI structure is built using a hybrid integrated platform of silicon and lithium niobate, while a suitable half-wave voltage is obtained by linear scanning, which realizes the conversion of the optical path. The output signal is simulated at different conversion frequencies and, accordingly, the frequency f is selected as 50 MHz. This significantly reduces the step fluctuation of the output current. Due to the small loss of the silicon-based Si_3N_4-waveguide, even if the radius

of the resonator is increased to obtain a larger Q value, the S factor will not be reduced significantly. At the same radius $R = 1000$ μm, the Q value of the silicon-based Si_3N_4 resonator is 1.58 times that of the SOI resonator, and the S factor is 1.62 times that of the latter. This shows advantages of the Si_3N_4 micro-ring resonator over SOI micro-ring resonators; the increase in the coupling coefficient k increases the coupling loss of the resonant cavity. Accordingly, as the Q value decreases, the output current exhibits a trend that first increases and then decreases. At the coupling coefficient $k = 0.2$, a large Q value and an output current can be simultaneously obtained, which improves the detection range. The system's simulation parameters are determined through the analysis of the above units, and the speed information is converted into phase information and loaded on the resonant cavity through a phase shifter to dynamically simulate the gyroscope system. Finally, by adding a $\pi/2$ phase offset to one of the rings, the problems linked to low sensitivity and inability to determine the direction of speed are solved. The research results of this work provide a theoretical reference for the development of an optical gyroscope with a silicon-based hybrid integrated micro-ring architecture.

Acknowledgments

Project supported by the science and technology general project of Beijing Municipal Education Commission (Grant No. KM202111232019), Beijing Municipal Natural Science Foundation (Grant No. 2214058), the Discipline Innovation Program of Higher Education (Grant No. D17021), the Open Project of the State Key Laboratory of Integrated Optoelectronics (Grant No. IOSKL2020KF22), Beijing Great Wall Scholars Program (Grant No. CIT&TCD20190323), the National Natural Science Foundation of China (Grant No. 61875237), and Beijing Youth Talent Support Program (Grant No. Z2019042).

References

[1] Zhang G C 2008 *The Principle and Technology of Fiber Optic Gyroscope* (Beijing: National Defence Industry Press) pp. 1–36
[2] Zhang Y S, Zhang C X, Feng L S, *et al.* 2017 *Optoelectronics and Optical Gyroscopes* (Beijing: Tsinghua University Press) pp. 513–519
[3] Liu D N, Qing C, Li H, *et al.* 2020 *The 4th National Autonomous Navigation Academic Conference–Technology and Application of Photonic Crystal Fiber Gyroscope and Related Devices*, December 11–15, 2020, Xi'an, China, pp. 9–14
[4] Feng L S, Wang X, Liu D N, *et al.* 2016 *Symposium on Development and Application of Optical Gyro and System Technology*, September 26–27, 2016, Jiangxi, China, pp. 72–76
[5] Bi F, Zhang D L, Lu L D, Zhu L Q 2021 *Laser & Optoelectronics Progress* **58** 7
[6] Dai D 2018 *Proc. IEEE* **106** 2117
[7] Lim A E J, Song J, Fang Q, *et al.* 2013 *IEEE J. Sel. Top. Quant. Electron.* **20** 405
[8] Talebifard S, Schmidt S, Shi W, *et al.* 2017 *Biomed. Opt. Express* **8** 500
[9] Ciminelli C, Dell'Olio F, Armenise M N, *et al.* 2013 *Opt. Express* **21** 556
[10] Spencer D T, Bauters J F, Heck M J, *et al.* 2014 *Optica* **1** 153
[11] Maiti R, Hemnani R A, Amin R, *et al.* 2019 *Nanophotonics* **8** 435
[12] Yin Y X, Yin X J, Zhang X P, *et al.* 2021 *Photonics* **8** 141
[13] Yu H Y, Zhang C X, Feng L S, Hong L F and Wang J J 2011 *Chin. Phys. Lett.* **28** 084203
[14] Ciminelli C, Campanella C E, Dell'Olio F, *et al.* 2013 *Journal of the European Optical Society-Rapid Publications* **8**
[15] Feng L, Wang J, Zhi Y, *et al.* 2014 *Opt. Express* **5** 158
[16] Khial P P, White A D, Hajimiri A 2018 *Nat. Photon.* **12** 671
[17] Mohammadi M, Olyaee S, Seifouri M 2019 *Silicon* **11** 2531
[18] Wu B B, Yu Y, Zhang X L 2019 *Sci. Rep.* **9** 1
[19] Zhang L, Jie L L, Zhang M, *et al.* 2020 *Photon. Res.* **8** 684
[20] Groote A D, Peters J D, Davenport M L, *et al.* 2014 *Opt. Lett.* **39** 4784
[21] Komljenovic T, Srinivasan S 2015 *IEEE J. Sel. Top. Quant. Electron.* **21** 214
[22] Zhang C, Srinivasan S, Tang Y M, *et al.* 2014 *Opt. Express* **22** 10202
[23] Chen L, Chen J, Nagy J, *et al.* 2015 *Opt. Express* **23** 13255
[24] He M, Xu M, Ren Y, *et al.* 2019 *Nat. Photon.* **13** 359
[25] Yu Q C, Liang X R, Ma W D 2020 *Opt. Commun. Technol.* **44** 37
[26] Bauters J F, Heck M J R, John D D, *et al.* 2011 *Opt. Express* **19** 24090
[27] Blumenthal, Daniel J, Heideman, *et al.* 2018 *Proc. IEEE* **106** 2209
[28] Post E J 1967 *Rev. Mod. Phys.* **39** 475
[29] Lu H W, Wei J T, Zhao H, *et al.* 2016 *Guangdong Communication Technology* **36** 76
[30] Li J Y, Lu D F and Qi Z M 2014 *J. Phys.* **63** 321
[31] Sun D X, Zhang D L, Bi F, *et al.* 2021 *Progress in Laser and Optoelectronics* **10** 1